Free-Standing Plasmonic-Nanorod Superlattice Sheets

Khee Chaw Ng,[†,§] **Indika B. Udagedara,**[‡] **Ivan D. Rukhlenko,**[‡] **Yi Chen,**[†] **Yue Tang,**[†,§] **Malin Premaratne,**[‡] **and Wenlong Cheng**[†,§,*]

[†]Department of Chemical Engineering, Faculty of Engineering, Monash University, Clayton 3800, Victoria, Australia, [‡]Advanced Computing and Simulation Laboratory (AχL), Department of Electrical and Computer Systems Engineering, Faculty of Engineering, Monash University, Clayton 3800, Victoria, Australia, and [§]The Melbourne Centre for Nanofabrication, 151 Wellington Road, Clayton 3168, Victoria, Australia

The self-assembly of monodisperse inorganic nanoparticles into highly ordered arrays (superlattices) constitutes an inexpensive bottom-up approach to materials and devices with new functions.[1−15] These functions are programmable by varying the size, shape, and composition of the nanoparticles, as well as the packing order of the assemblies.[16] To date, a variety of building blocks—including metal, semiconductor, and magnetic nanoparticles—have been successfully used to create superlattices with properties different from those of the corresponding bulk materials, dispersed constituents, or disordered assemblies.[6,8,9,11] The surface-capping ligands play a crucial role "directing" self-assembly in the formation of high-quality superlattices.[17,18] Recently, substantial advances have been made in the utilization of DNA, alkyl, and polymer ligands to rationally tailor interparticle potential by Watson−Crick base-pairing, entropic, and electrostatic forces.[5] It is clear that control over these nanoscale forces enables researchers to program multicomponent superlattices into a variety of crystalline structures, because of the acquired liberty in adjusting chemical composition, size, and stoichiometry of the constituent nanoparticles.[19−24] Notably, the ligand-based self-assembly methods can be combined with top-down lithographical techniques, leading to an assortment of patterned superlattice structures.[6,7] Moreover, recently developed methodologies even allow the formation of large-scale, transferable, free-standing superlattice sheets (or membranes), representing a step toward the integration of superlattices into practical devices.[3,6,19,25−27]

In contrast to the significant progress achieved in the construction of superlattices from nanospheres, much less success has been reported for nonspherical building

ABSTRACT
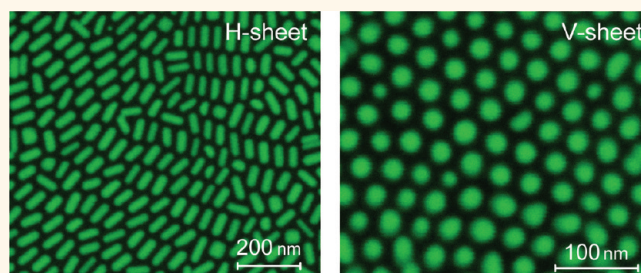
The self-assembly of monodisperse inorganic nanoparticles into highly ordered arrays (superlattices) represents an exciting route to materials and devices with new functions. It allows programming their properties by varying the size, shape, and composition of the nanoparticles, as well as the packing order of the assemblies. While substantial progress has been achieved in the fabrication of superlattice materials made of nanospheres, limited advances have been made in growing similar materials with anisotropic building blocks, which is particularly true for free-standing two-dimensional superlattices. In this paper, we report the controlled growth of free-standing, large-area, monolayered gold-nanorod superlattice sheets by polymer ligands in an entropy-driven interfacial self-assembly process. Furthermore, we experimentally characterize the plasmonic properties of horizontally aligned sheets (H-sheets) and vertically aligned sheets (V-sheets) and show that observed features can be well described using a theoretical model based on the discrete-dipole approximation. Our polymer-ligand-based strategy may be extended to other anisotropic plasmonic building blocks, offering a robust and inexpensive avenue to plasmonic nanosheets for various applications in nanophotonic devices and sensors.

KEYWORDS: nanorods · self-assembly · superlattice sheets · polymer ligands · plasmonics

blocks until recently.[28−31] Previously, pristine gold nanorods (GNRs) have been found to form two-dimensional (2D) and three-dimensional (3D) superlattices on solid substrates.[1,32,33] Here, we report on the synthesis of large-area, free-standing nanorod superlattice sheets using polymer as ligands in a drying-mediated self-assembly process at the air−water interface, which is an extension of our previous success[26] from
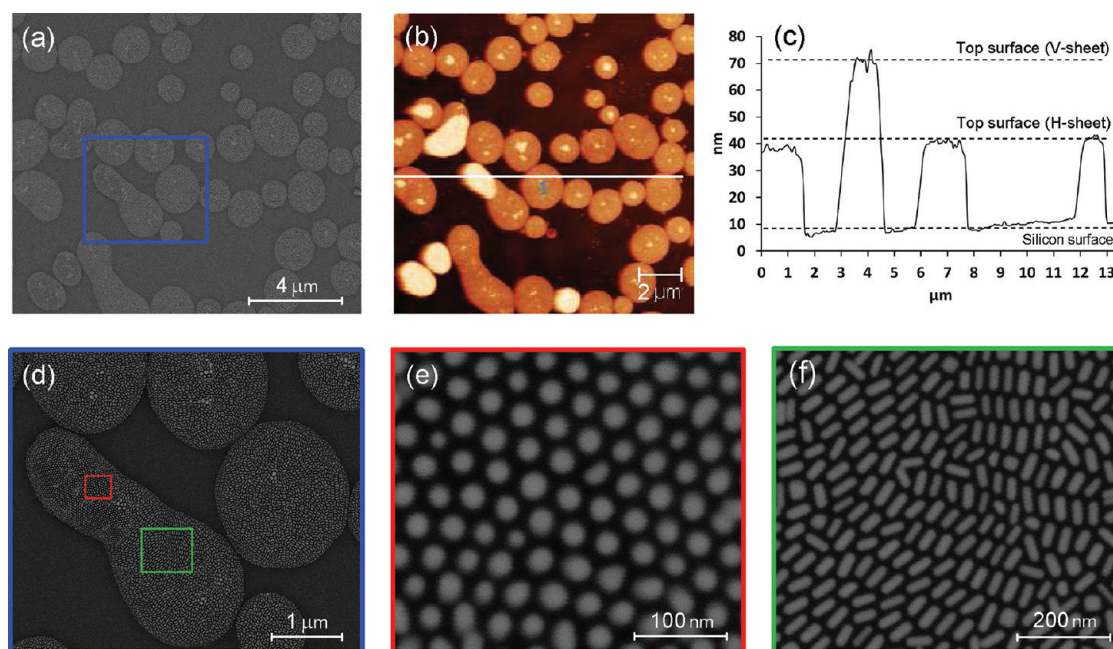
Figure 1. (a) SEM images of circular H- and V-sheets of PS-GNRs self-assembled at the air−water interface and (b) the corresponding AFM micrographs of the sheets on a silicon wafer. (c) Representative AFM height profile marked by the horizontal line in panel (b). (d)−(f) Magnified SEM images of panel (a) reveal that both sheets are ordered, flat monolayers of GNRs that are well-spaced by polystyrene ligands. The length, diameter, and aspect ratio of GNRs are L = 54.1 ± 5.7 nm, d = 21.2 ± 3.5 nm, L/d = 2.6 ± 0.4; the number average molecular weight and average length of ligands are 20 000 g/mol and 4.9 nm; the thicknesses of the H- and V-sheets are 31.3 ± 0.3 and 63.6 ± 2.1 nm.

spheres to nanorods. Detailed structural characterization demonstrates that GNRs can align either horizontally into superlattice monolayer sheets (H-sheets) or vertically into superlattice monolayer sheets (V-sheets). The two types of sheets exhibit distinct plasmonic properties, as characterized by a microscope UV−visible (UV−vis) spectrophotometer. By applying discrete-dipole-approximation (DDA) modeling to describe the nanorod superlattices, we reveal the plasmonic mechanisms behind their optical response. Our polymer-ligand-based strategy may be extended to free-standing superlattices made of other anisotropic building blocks, thus serving as a promising general approach to the synthesis of structurally well-defined plasmonic nanosheets for various applications in nanophotonic devices and sensors.

RESULTS AND DISCUSSION

Polystyrene-capped gold nanorods (PS-GNRs) were obtained using a two-step grafting procedure similar to the one used for the spherical nanoparticles.[26] At first, aqueous hexadecyltrimethylammonium bromide-capped GNRs (CTAB-GNRs) were synthesized using the well-established seed-mediated approach.[34] Then, thiolated polystyrene ligands ($\bar{M}_n$ = 20 000 g/mol) were introduced, which led to the replacement of the weaker-binding CTAB molecules, rendering nanorods hydrophobic and soluble only in organic media. The PS-GNRs are highly stable and free of aggregation, exhibiting two well-pronounced plasmon resonances

(Figure S1): (i) transverse surface plasmon resonance (TSPR) and (ii) longitudinal surface plasmon resonance (LSPR). The LSPR of PS-GNRs dispersed in chloroform is red-shifted by about 30 nm with respect to the same resonance of CTAB-GNRs in water, due to the increased refractive index of the solution.[35]

To form GNR superlattices, a drop of 5 μL of PS-GNR−chloroform solution was spread onto the water surface with an area of ∼10 cm^2 at ambient temperature. Immediately after that, the system was sealed by capping the beaker with a lid, in order to prevent rapid solvent evaporation. Five minutes later, gold reflective membranes float on the water subphase, indicative of the complete solidification. Using a horizontal liftoff technique, the membranes were transferred onto a number of different substrates, including transmission electron microscope (TEM) grids, glass slides, and silicon chips.

Comprehensive morphological characterization demonstrates that PS-GNRs are self-assembled into superlattice monolayer sheets with either horizontally or vertically aligned packing (i.e., H- or V-sheets). We characterize a sample of coexisting H- and V-sheets first using a scanning electron microscope (SEM) and subsequently address the same area with an atomic force microscope (AFM) to further prove the two distinct packing orders. The corresponding SEM and AFM images are shown in Figure 1a and b. Both show that superlattice sheets are circular in shape, with lateral sizes of a few micrometers, similar to the
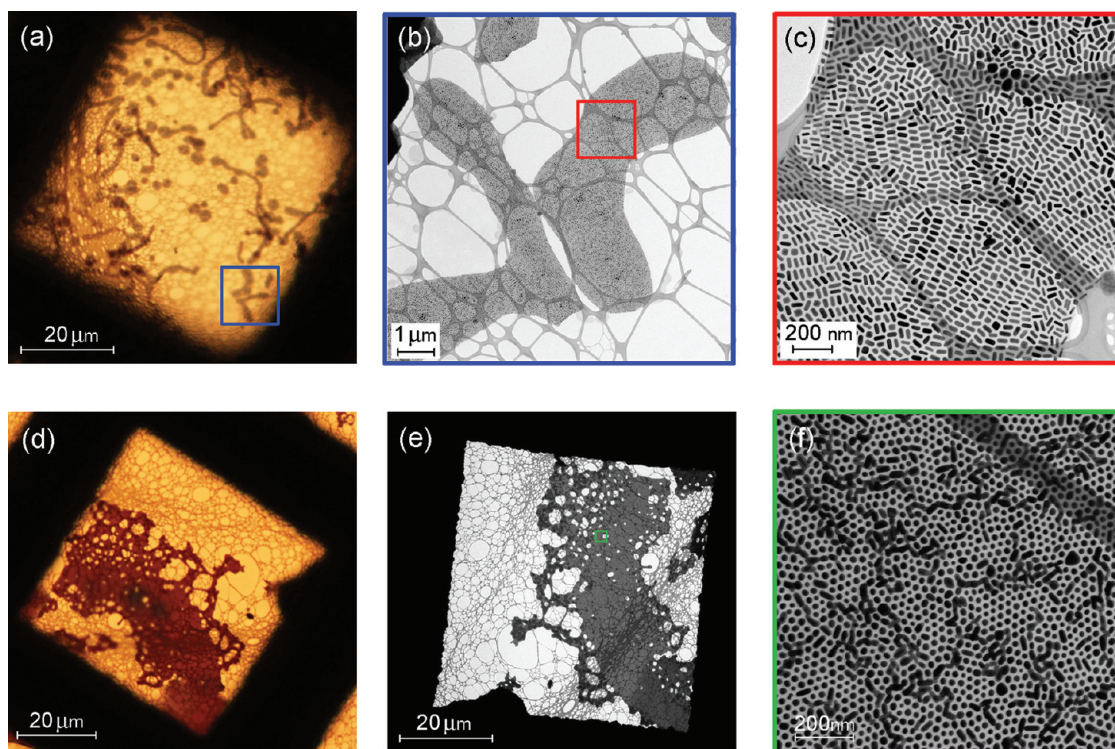
Figure 2. Optical microscopy images and the corresponding TEM micrographs of free-standing, noncircular (a−c) H-sheets and (d−f) V-sheets suspended on 57 × 57 μm^2 holey lacey carbon TEM grids. In the (b) belt-shaped H-sheets and (e) irregular-shaped V-sheet, PS-GNRs are aligned (c) horizontally and (f) vertically with respect to the TEM grid. The dimensions of GNRs and parameters of ligands are the same as in Figure 1.

previously reported case of superlattices composed of nanospheres.[26] The AFM line-scan profile in Figure 1c demonstrates that lighter domains in Figure 1b correspond to V-sheets, whereas darker domains correspond to H-sheets. The high-resolution SEM images in Figure 1e and f show that GNRs are hexagonally packed in V-sheets and form nematic phases in H-sheets. In the V-sheets, the nanorods are often aligned horizontally at the edge (Figure S2), which is consistent with the previous observation by Weller *et al.*[36] From a set of AFM line-scan measurements, the thicknesses of H- and V-sheets are estimated to be 31.3 ± 0.3 and 63.6 ± 2.1 nm, respectively. After subtracting width and length of the nanorods, the polystyrene brush heights at their sides and ends are estimated to be about 5.0 and 4.7 nm, respectively. The smaller brush height at the ends of GNRs is likely due to the curvature effects.

We attribute the formation of GNR superlattices to an entropy-driven self-assembly confined to the 2D air−water interface. In a dilute solution of sufficiently low GNR concentrations, the rods are free to take on any possible orientations and positions to achieve maximum entropy. However, both translational and orientational freedoms of the rods are restricted when their concentration increases as a result of chloroform evaporation. In order to maximize the total entropy of the system, the rods sacrifice some of their orientational freedom in exchange for increasing translation freedom by aligning parallel to each other, thereby minimizing the excluded volume and free energy.

The assembly pattern depends on the operating temperature. At ambient temperatures, the majority of the sheets are H-sheets. As the temperature or annealing time under the chloroform atmosphere is increased, the yield of V-sheets improves. This behavior is similar to that reported previously for semiconductor nanorods.[18,36,37] For the same batch of PS-GNRs, predominantly H-sheets are obtained at 23 °C, whereas the majority of V-sheets in the sample are obtained after its two-hour aging at 60 °C in the chloroform atmosphere (Figure S3). This could be explained by the application of Tirado's model,[38] which states that the rotational and translation diffusion constants of cylindrical objects in the solution are proportional to the ratio of temperature to shear viscosity. Since the shear viscosity decreases with temperature, the diffusion constants exhibit the same dependency. This effectively gives the system more time to lower its free energy to correct kinetically trapped disordered structures, reaching their most thermodynamically stable state, associated with vertical alignment of GNRs.

Besides temperature, the packing order and quality of the nanorod sheets are dependent on the length of the polymer ligands. The softness argument[17] predicts that longer molecular ligands are needed to form superlattices from larger nanoparticles. Consistent with this argument, we observed a poor ordering when
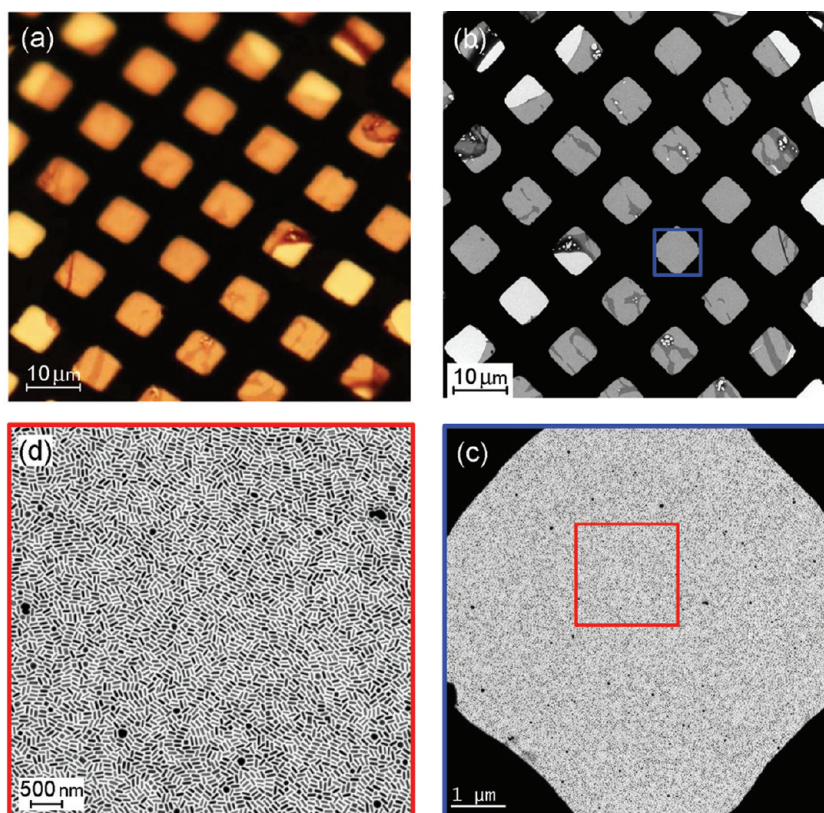
Figure 3. Large-scale structures of free-standing H-sheets fabricated upon evaporating water droplets sitting on holey square carbon TEM grids: (a) optical-microscopy image and (b) the corresponding TEM micrograph of the sheets exclusively suspended over $7 \times 7 \ \mu m^2$ microholes. Panels (c) and (d) show the magnified parts of the sheet in panel (b), consisting of well-separated PS-GNRs throughout the entire hole. The dimensions of GNRs are $L = 51.8 \pm 8.8$ nm, $d = 16.5 \pm 3.3$ nm, and $L/d = 3.1 \pm 0.4$.

shorter polystyrene ligands were used. For example, for polystyrene ligands with $\bar{M}_h = 12\,000$ g/mol, we did not obtain ordered, uniform sheets, but observed the formation of cracked, multistacked, and disordered structures (Figure S4). This is because van der Waals attraction forces outweigh the steric hindrance of ligands, leading to unbalanced interparticle interaction.

In addition to circular H- and V-sheets, we also observed other shapes, such as belts or irregular shapes seen in Figure 2a−f. These sheets seem to be developed from merging circular sheets due to localized high lateral drying forces during the self-assembly process. It is important to grow large, pure superlattice sheets for optical studies. To grow large sheets, we used a droplet-based interfacial self-assembly strategy reported by Muggenburg et al.[9] By spreading a PS-GNR−chloroform solution across a water droplet sitting on a holey substrate, we found that PS-GNRs may self-assemble into superlattice sheets with lateral dimensions of over 100 μm (see Figure 3). The formation of large sheets is likely due to the strong surface tension of water, leading small sheets to merge into large ones.

The degree of order for the large H-sheets can be quantified using Hore's method[39] by calculating the orientational-order parameter

$$S_{2D} = \frac{1}{N_{rod}} \sum_{j=1}^{N_{rod}} \cos 2\vartheta_j$$

where ϑ_j is the angle between the jth GNR and the average orientation of GNRs in a region of radius r around it, and N_{rod} is the total number of GNRs in that region. In a large H-sheet of a few hundred micrometers in size, we randomly select three circular regions for analysis, as shown in Figure 4a. For each region, the 2D ordering parameters are calculated with $r = 0.05, 0.1, ..., 1.2 \ \mu m$ and plotted in Figure 4c. Evidently, the ordering parameter has a weak dependence on the scale of scrutiny with an average value of about 45%. In some areas, like those shown in Figure 4b, the superlattice sheets are folded and partially attached to the holey substrate (Figure S5). The ordering parameter in such areas is enhanced compared to that in the fully attached sheets (compare Figure 4d and c), which can be explained by stress relaxation, a phenomenon observed previously for DNA−nanoparticle sheets.[6]

We further investigate the optical properties of H- and V-sheets shown in Figure 5a and b with the microscope UV−visible spectrophotometer. The
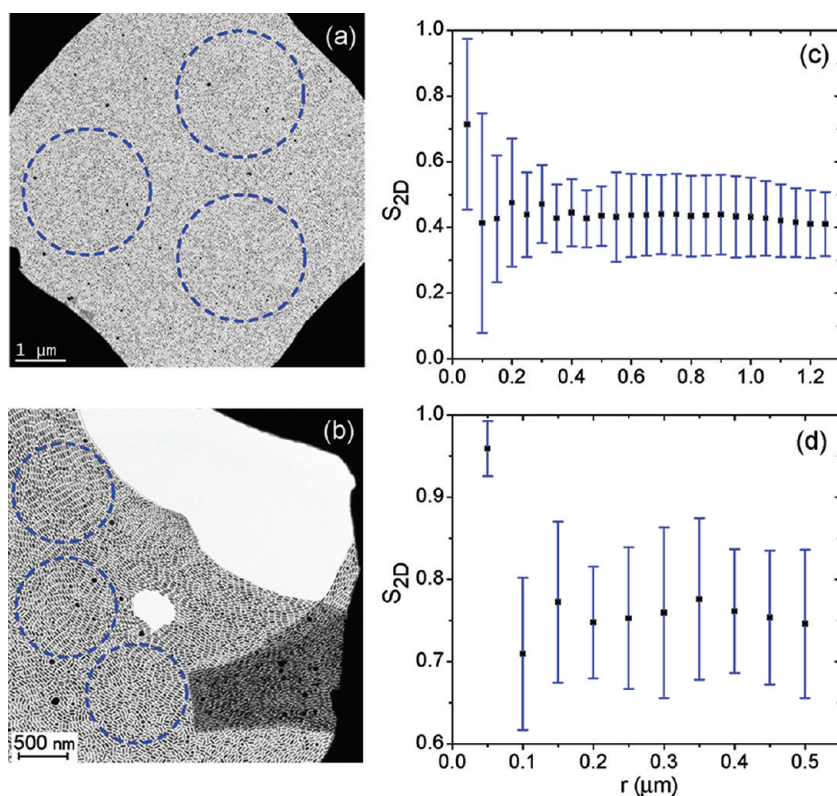
Figure 4. TEM micrographs of H-sheets (a) fully and (b) partially attached to holey square carbon TEM grids. (c and d) Plots of 2D orientational-order parameters *versus* the radius of the analyzed region. The dashed circles in panels (a) and (b) show the regions of radii 1.25 and 0.5 μm selected for calculating the ordering parameter. The parameters of PS-GNRs are the same as in Figure 3.

resulting spectra are shown in Figure 5c and d. It is seen that the spectrum of the H-sheet features two resonant peaks (TSPR and LSPR), while only a single peak (TSPR) is exhibited by the V-sheet, because longitudinal plasmons are not excited on the vertically aligned GNRs. In both cases, the peaks are red-shifted with respect to those of isolated PS-GNRs.

A deeper insight into the characteristics of the PS-GNR sheets may be obtained through theoretical modeling of their optical response. Even with the availability of extensive computing resources, carrying out light-scattering calculations for the entire super-lattice is generally not feasible due to the exceptionally high computational cost. Fortunately, owing to the quasi-periodic nature of the GNR sheets, we may employ efficient numerical techniques—such as DDA or the finite-difference time-domain (FDTD) method—developed for the calculation of scattering from periodic systems.[40,41] We chose the DDA method over the FDTD method because of its computational efficiency for calculating the scattering of light by particles with irregular shapes.[42,43]

We first model optical behavior of a single GNR in a chloroform solution, which corresponds to the situation where GNRs are spaced far apart and their interaction is negligible. Different orientation of GNRs with respect to the excitation electric field results in two

plasmon resonances, while the size distribution of GNRs leads to the inhomogeneous broadening of the extinction spectrum. Consideration of these effects in modeling enables us to adequately predict the shape and position of the TSPR and LSPR in the experimental spectrum (Figures S6 and S7). The interaction between different GNRs cannot be ignored if they are closely packed, as occurs in the sheets in Figures 1−5. It depends on the distance between the GNRs and their mutual orientations, the distribution of which gives rise to further broadening of the plasmon resonances compared to the resonances of noninteracting GNRs.

The optical response of a sheet with closely spaced GNRs may be found by treating the sheet as a super-position of periodic lattices with fixed GNR dimensions and spacing. We calculate first the extinction spectra for a set of such lattices with rectangular unit cells of different sizes. The spectra of these lattices are then averaged according to their weights, determined by the size and space distributions of GNRs (Figures S8 and S9). In Figure 6a, we plot the thus calculated extinction spectra for the H-sheet. It is seen that the TSPR near 530 nm is correctly predicted by the DDA method, while the 855 nm LSPR is estimated to be near 826 nm. The numerically obtained 530 nm peak is weaker and less broadened than the experimental one, which is mainly due to the employment of
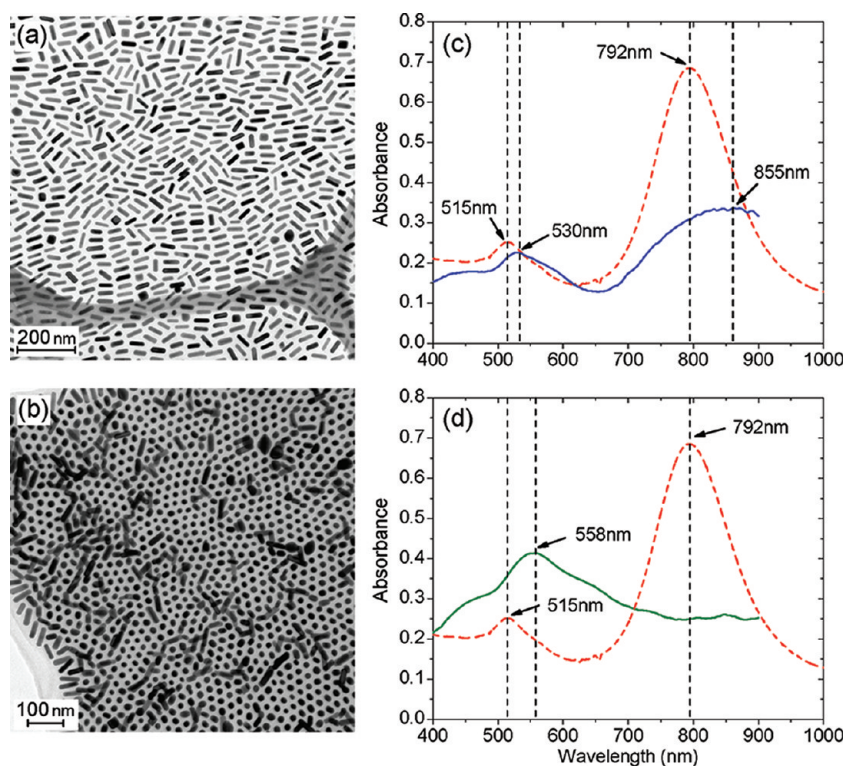
Figure 5. TEM micrographs of free-standing (a) H-sheet and (b) V-sheet and (c and d) the corresponding UV−vis spectroscopic data. The solid and dashed curves correspond to the spectra of the sheets and dilute PS-GNR solution, respectively. The parameters of PS-GNRs are the same as in Figure 3.
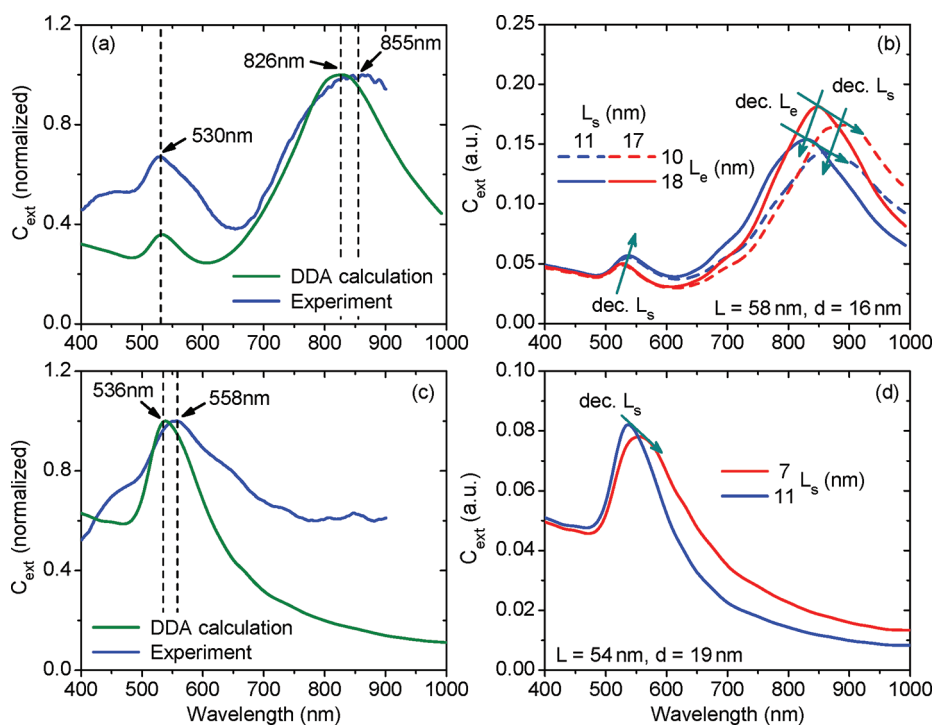

Figure 6. Extinction spectra of (a) H-sheet and (c) V-sheet obtained experimentally (blue curves) and with the DDA method (green curves). The spectra are normalized by their peak values. Theoretical extinction spectra of (b) four H-sheets with different end-to-end spacing L_e and side-by-side spacing L_s of GNRs and (d) two V-sheets of different L_s. In both cases, the length L and diameter d of GNRs are fixed. Arrows indicate the trends of the resonances when L_e and L_s are decreased.

approximate size and space distributions for GNRs. The effect of the nanorods' spacing on extinction is illustrated by Figure 6b, where we plot extinction spectra of four periodic lattices made of constant-size GNRs.

One can see that a decrease in the end-to-end spacing L_e of nanorods red-shifts the LSPR, while the blue-shift of the same resonance occurs upon decreasing the side-by-side nanorod spacing L_s. In contrast, the TSPR position is predominantly affected by the change in L_s and is almost insensitive to the variation of L_e.

Figure 6c shows the numerically calculated extinction spectrum for a GNR V-sheet. Prediction of the spectral position of TSPR by the DDA method is seen to be reasonably accurate, with only a small deviation of the peak position from the experimental one. The decrease in L_s results in red-shifting and broadening of the resonance peak, as indicated by Figure 6d. The reason that the theoretical spectrum in Figure 6c deviates from the experimental one may therefore be partially attributed to the nanorods being located slightly closer to each other than it was assumed in the simulations.

CONCLUSION

We have demonstrated a simple yet robust polymer-ligand-based approach to assemble plasmonic gold nanorods into two types of ordered superlattice sheets, namely, H-sheets and V-sheets. Both sheets can be controlled at the monolayer level with lateral dimensions in the submillimeter scale. The nanosheets display distinct spectral features dependent on the nanorod orientations, spacing, and size. These features are explained by the difference in plasmon modes excited on the sheets, which is confirmed through DDA calculations. Plasmon hybridization theory[44] predicts that plasmons on neighboring metallic nanostructures interact, mix, and hybridize just like the electronic wave functions of simple atomic and molecular orbitals. According to this theory, plasmonic superlattice sheets are a new class of 2D optical materials in which light can be engineered without diffraction limit by exciting, directing, and manipulating plasmons. Such novel 2D optical materials can have a broad spectrum of technical applications. For example, hot spots in the plasmonic superlattices may be used for ultrasensitive Raman sensors in medical diagnosis; enhanced optical density of states near particle surfaces can provide control over the color, directionality, and polarization of light-emitting diodes; 2D plasmonic sheets may also be used as efficient color filters, waveguides, and light enhancers in solar cells. Given the generality of the polymer-conjugation reactions and interfacial self-assembly process employed in our method, we believe our strategy possesses modularity, extendable to other anisotropic-nanoparticle systems. This will potentially open a new route to engineer free-standing plasmonic nanosheets for a number of technical applications in optoelectronic devices and sensors.

METHODS

Materials. Holey lacey/Formvar carbon, 300-mesh copper grids were purchased from Ted Pella. Quantifoil holey carbon films with $7 \times 7 \ \mu m^2$ square holes were purchased from Electron Microscopy Sciences. A water bath (model: AquaBath) was purchased from Thermo Fisher Scientific Australia. Gold(III) chloride trihydrate ($HAuCl_4$), hexadecyltrimethylammonium bromide (CTAB), silver nitrate ($AgNO_3$), sodium borohydride ($NaBH_4$), and L-ascorbic acid were obtained from Sigma Aldrich. Tetrahydrofuran (THF) and chloroform were obtained from Merck KGaA. Thiol-functionalized polystyrene ($\bar{M}_n = 12\,000$ g/mol and $\bar{M}_n = 20\,000$ g/mol, $\bar{M}_w/\bar{M}_n = 1.09$) was purchased from Polymer Source Inc.

Synthesis of CTAB-GNRs. GNRs capped with CTAB were prepared according to the well-established seed-mediated growth method.[34] At first, a seed solution was prepared by gently stirring CTAB (5.0 mL, 0.2 M) and $HAuCl_4$ (5.0 mL, 0.5 mM) at low speed. Then, ice-cold $NaBH_4$ (0.6 mL, 0.01 M) was added into the mixture followed by a three-minute vigorous stirring. The solution turned brownish-yellow immediately with the addition of $NaBH_4$. The seed solution was then aged at 25 °C before seeding to growth solution. Growth solution was prepared by adding CTAB (5.0 mL, 0.2 M) into $AgNO_3$ solution (4 mM), followed by $HAuCl_4$ (5.0 mL, 1.0 mM) and ascorbic acid (0.07 mL, 0.0788 M). Addition of ascorbic acid changed the yellowish mixture to colorless. To grow anisotropic CTAB-capped GNRs, 12 μL of premade seed was added into the growth solution and aged at 30 °C for two hours. Gold nanorods with various initial mean aspect ratios were synthesized by changing the amount of $AgNO_3$ ranging from 150 to 250 μL. The initial concentration of GNRs was estimated through the correlation of the nanorod aspect ratio to the plasmon band extinction coefficient.[45]

Synthesis of PS-GNRs. PS-GNRs were prepared following a modified grafting approach.[26,46,47] Typically, the as-prepared CTAB-GNR solution was spun down to 30 μL, 55 nM by three 12 min centrifugations at 12 krpm each. The concentrated CTAB-GNR solution was then mixed with 1 mL of PS-SH-THF solution (1.5 mg/mL) under vigorous agitation. The mixture was aged for a day under room temperature to allow for a complete ligand exchange reaction. High-quality PS-GNRs were then obtained through a single 10 min centrifugation of the PS-GNR-THF solution at 10 krpm, followed by the resuspension in chloroform.

Fabrication of GNR Superlattice Sheets. In the fabrication of H-sheets at air−water interfaces, a drop of 5 μL of PS-GNR-chloroform solution (from about 20 to 60 nM) was put carefully into a $\sim$10 cm^2 glass beaker containing water at ambient temperature. After the addition of PS-GNR-chloroform solution, a lid was immediately placed on the beaker to prevent fluid flows and rapid evaporation. The presence of reflective gold floating films on the water subphase indicated the complete solidification. Using a horizontal liftoff technique, the monolayers on the water subphase were transferred to TEM holey lacey grids. To increase the yield of V-sheets, 5 μL of PS-GNR-chloroform solution (about 57 nM) was inserted into a $\sim$10 cm^2 glass beaker containing water in a 60 °C water bath. Annealing was performed in the enclosed water bath for two hours before collecting the sample onto lacey TEM grids. Additionally, the yield of V-sheets was enhanced by two hours of annealing in the chloroform atmosphere at 60 °C. To form larger H-sheets, 0.5 μL of PS-GNRs (about 66 nM) was carefully spread on a water droplet sitting on quantifoil holey carbon film with square holes. Before the addition of PS-GNRs, the layer of water droplet was formed on the grids through vertically immersing the grid into mili-Q water at ambient temperature.

Characterization of GNR Sheets. An Agilent 8453 UV−vis spectrophotometer was used to determine optical absorption spectra of CTAB-GNRs in water and PS-GNRs in chloroform. A quartz cuvette was used during the UV−vis measurement of PS-GNRs

in chloroform. UV–vis spectra of free-standing GNR sheets were obtained using a J&M MSP210 microscope spectrometry system, while the films were illuminated by a high-intensity fiber light source under a 40× objective. The spectra were acquired based on sheets that were free-standing over the holes of the lacey grids. The morphologies of the sheets were determined by Hitachi H-7500 field emission TEM operating at 80 kV, and FEI Nova NanoSEM 430 field emission gun SEM operating at 5 kV. The sheets were able to withstand high electron-beam irradiation in high vacuum without deformation. Optical images of the sheets were acquired by a Nikon Industrial bright field ECLIPSE LV 100D microscope under transmission mode. AFM micrographs were obtained through a Veeco Dimension Icon scanning probe microscope at 25 °C in a tapping mode using PointProbe-Plus ZEILR silicon probes (nanosensors). The sheets' height profile was characterized using Gwyddion software. The characterization of the GNRs' dimensions was conducted by an image-analysis program, Image-Pro Plus version 6.2.

Numerical Modeling. To calculate the extinction spectrum of GNR sheets, we use the DDA code DDSCAT, which was made freely available by Draine and Flatau.[48] The DDA method is based on representing the scatterer by an assembly of point dipoles with properly assigned isotropic polarizabilities.[49,50] This representation allows one to describe the scatterer's interaction with the electric field of incident light by a set of coupled linear equations, whose solutions yield the moments induced on the dipoles constituting the scatterer. In the case of periodically arranged scatters, only equations for the dipoles in the unit cell need to be solved.

Consider an aggregate of identical scatterers periodically arranged in a 2D rectangular lattice, in which their positions are determined by the vectors $\mathbf{a}_{mn} = m\mathbf{u} + n\mathbf{v}$, where $m,n \in Z$ and $\mathbf{u}$ and $\mathbf{v}$ are the primitive translation vectors of the lattice, which are assumed to be nonparallel to each other. Let the scatterer in the unit cell $\mathbf{a}_{00}$ be represented by the N dipoles $\mathbf{p}_j^{00}$ ($j = 1, ..., N$) with polarizability α. The jth dipole located at the point characterized by the radius vector $\mathbf{r}_j$ is related to the local electrical field strength $\mathbf{E}_{local}(\mathbf{r}_j)$ at this point as

$$\mathbf{p}_j^{00} = \alpha \mathbf{E}_{local}(\mathbf{r}_j) \tag{1}$$

Suppose that the electrical field incident on this dipole is a plane wave of the form $\mathbf{E}(\mathbf{r}_j) = \mathbf{E}_0 \exp(i\mathbf{k}\mathbf{r}_j)$, where $\mathbf{k}$ is the wave vector. Then, the local field seen by the jth dipole is a superposition of the incident field $\mathbf{E}(\mathbf{r}_j)$ and the field generated by all other dipoles,

$$\mathbf{E}_{local}(\mathbf{r}_j) = \mathbf{E}_0 \exp(i\mathbf{k}\mathbf{r}_j) + \sum_{l=1}^{N}\sum_{m=-\infty}^{+\infty}\sum_{n=-\infty}^{+\infty}(1 - \delta_{jl}\delta_{m0}\delta_{n0})A_{jl}^{mn}\mathbf{p}_l^{mn} \tag{2}$$

where δ_{ik} is the Kronecker delta and elements $A_{jl}^{mn}\mathbf{p}_l^{mn}$ represent the electric field generated by a lth dipole constituting the scatter in the cell characterized by the vector $\mathbf{a}_{mn}$. Explicit expressions for A_{jl}^{mn} are well known and can be found elsewhere.[51] Substitution of eq 1 for eq 2 gives the following self-consistent equations that need to be solved to find the electrical field distribution in the lattice:

$$\alpha^{-1}\mathbf{p}_j^{00} - \sum_{l=1}^{N}\sum_{m=-\infty}^{+\infty}\sum_{n=-\infty}^{+\infty}(1 - \delta_{jl}\delta_{m0}\delta_{n0})A_{jl}^{mn}\mathbf{p}_l^{mn}$$
$$= \mathbf{E}_0 \exp(i\mathbf{k}\mathbf{r}_j)$$

Owing to the periodicity of the lattice, $\mathbf{p}_j^{mn} = \mathbf{p}_j^{00}\exp(i\mathbf{k}\mathbf{a}_{mn})$, and the above equation can be rewritten in terms of the dipoles of a single scatterer. After that, the infinite sums may be truncated by an appropriately converging function and the unknown dipole moments may be calculated from the resulting set of linear algebraic equations.[42,52] The extinction cross section of the system is finally given by

$$C_{ext} = \frac{4\pi|\mathbf{k}|}{|\mathbf{E}_0|^2}\sum_{j=1}^{N}Im[\mathbf{E}^*(\mathbf{r}_j)\mathbf{p}_j^{00}]$$

In order to calculate the extinction spectra of PS-GNRs dispersed in chloroform, we take into account both the arbitrariness of the GNRs' orientation and randomness of light polarization. This is accomplished in three stages. In the first stage, we calculate the extinction of a single-standing PS-GNR oriented either perpendicular or parallel to a linearly polarized light beam. In the next stage, we take the average of the resulting spectra with proper weights.[53] The homogeneously broadened extinction spectrum of the GNR ensemble is obtained in the third stage, by averaging a set of the orientation- and polarization-corrected spectra over the size distribution of GNRs (Figures S6 and S7). Since the mean distance between single-standing GNRs is much larger than the thicknesses of the polystyrene coatings, we neglect in this calculation the contribution of the polystyrene to the background refractive index and assume it to be equal to the refractive index of chloroform ($n = 1.45$).

It is well known that metals confined to nanovolumes feature high collision rates of free electrons due to the enhanced surface scattering.[54] Incorporation of this effect into the computational model shows that additional broadening occurs for both longitudinal and transverse resonances (Figure S6). It also reveals that the surface scattering has little effect on the positions of the plasmon resonances, thus enabling us to ignore the size-dependent change in permittivity and carry out calculations using the permittivity of bulk gold.[55] However, it must be noted that the surface scattering correction is typically required for accurate prediction of the extinction peaks where the characteristic size of GNRs is below 5 nm.[53,54,56]

To model the optical response of GNR sheets, we perform a series of DDA calculations by considering different rectangular lattices. The unit cell of a given lattice is comprised of a single GNR, placed at the cell's center horizontally for the H-sheet and vertically for the V-sheet. For the H-sheet, the translation vector of the lattice is specified by the side-by-side and end-to-end spacings of GNRs (L_s and L_e) and the length and width of GNRs (L and d). For the V-sheet it is specified by the parameters L_s and d. To account for the unpolarized light in the experiment with the H-sheet, two calculations are carried out for each set of parameters L_s, L_e, L, and d, with the rectangular unit cell being aligned perpendicular or parallel to the electric field of a linearly polarized light beam; the results of these calculations are then averaged with the weights of 1/3 and 2/3. Once the spectra are determined for all sets of parameters, they are weighted by the size and space distributions of GNRs to obtain the final spectrum (Figure S8). A similar procedure is followed for the V-sheet, except that only a single calculation is carried out for each pair of the parameters L_s and d (Figure S9). In both H- and V-sheets, the polystyrene coatings of different GNRs almost touch each other. Therefore, we take the refractive index of polystyrene ($n = 1.55$) as the refractive index of the background medium.

Supporting Information Available: Normalized UV–vis spectra of CTAB-GNRs in water and PS-GNRs in chloroform (Figure S1), TEM images of free-standing V-sheet (Figure S2), TEM images of H- and V-sheets formed under various conditions (Figure S3), TEM images of free-standing H-sheets self-assembled from GNRs capped with short polystyrene ligands (Figure S4), optical-microscopy and TEM images of folded H-sheets (Figure S5), numerically calculated extinction spectra of PS-GNRs in a chloroform solution (Figure S6), PS-GNR size distribution in a chloroform solution (Figure S7), PS-GNR size and spacing distributions in an H-sheet (Figure S8), and PS-GNR size and spacing distributions in a V-sheet (Figure S9). This material is available free of charge *via* the Internet at http://pubs.acs.org.

REFERENCES AND NOTES

1. Tan, S. J.; Campolongo, M. J.; Luo, D.; Cheng, W. Building Plasmonic Nanostructures with DNA. *Nat. Nanotechnol.* **2011**, *6*, 268–276.

2. He, J.; Lin, X.-M.; Chan, H.; Vukovic, L.; Kral, P.; Jaeger, H. M. Diffusion and Filtration Properties of Self-assembled Gold Nanocrystal Membranes. *Nano Lett.* **2011**, *11*, 2430–2435.

3. Dong, A.; Chen, J.; Vora, P. M.; Kikkawa, J. M.; Murray, C. B. Binary Nanocrystal Superlattice Membranes Self-assembled at the Liquid−Air Interface. *Nature* **2010**, *466*, 474–477.

4. Talapin, D. V.; Lee, J. S.; Kovalenko, M. V.; Shevchenko, E. V. Prospects of Colloidal Nanocrystals for Electronic and Optoelectronic Applications. *Chem. Rev.* **2010**, *110*, 389–458.

5. Bishop, K. J. M.; Wilmer, C. E.; Soh, S.; Grzybowski, B. A. Nanoscale Forces and Their Uses in Self-Assembly. *Small* **2009**, *5*, 1600–1630.

6. Cheng, W.; Campolongo, M. J.; Cha, J. J.; Tan, S. J.; Umbach, C. C.; Muller, D. A.; Luo, D. Free-standing Nanoparticle Superlattice Sheets Controlled by DNA. *Nat. Mater.* **2009**, *8*, 519–525.

7. Cheng, W.; Park, N.; Walter, M. T.; Hartman, M. R.; Luo, D. Nanopatterning Self-assembled Nanoparticle Superlattices by Moulding Microdroplets. *Nat. Nanotechnol.* **2008**, *3*, 682–690.

8. Urban, J. J.; Talapin, D. V.; Shevchenko, E. V.; Kagan, C. R.; Murray, C. B. Synergism in Binary Nanocrystal Superlattices Leads to Enhanced P-Type Conductivity in Self-assembled PbTe/Ag$_2$Te Thin Films. *Nat. Mater.* **2007**, *6*, 115–121.

9. Mueggenburg, K. E.; Lin, X. M.; Goldsmith, R. H.; Jaeger, H. M. Elastic Membranes of Close-packed Nanoparticle Arrays. *Nat. Mater.* **2007**, *6*, 656–660.

10. Tang, Z.; Zhang, Z.; Wang, Y.; Glotzer, S. C.; Kotov, N. A. Self-Assembly of CdTe Nanocrystals into Free-floating Sheets. *Science* **2006**, *314*, 274–278.

11. Courty, A.; Mermet, A.; Albouy, P. A.; Duval, E.; Pileni, M. P. Vibrational Coherence of Self-organized Silver Nanocrystals in F.C.C. Supra-Crystals. *Nat. Mater.* **2005**, *4*, 395–398.

12. Zhu, Z.; Meng, H.; Liu, W.; Liu, X.; Gong, J.; Qiu, X.; Jiang, L.; Wang, D.; Tang, Z. Superstructures and SERS Properties of Gold Nanocrystals with Different Shapes. *Angew. Chem., Int. Ed.* **2011**, *50*, 1593–1596.

13. Gao, Y.; Tang, Z. Design and Application of Inorganic Nanoparticle Superstructures: Current Status and Future Challenges. *Small* **2011**, *7*, 2133–2146.

14. Zeng, H.; Li, J.; Liu, J. P.; Wang, Z. L.; Sun, S. Exchange-coupled Nanocomposite Magnets by Nanoparticle Self-Assembly. *Nature* **2002**, *420*, 395–398.

15. Collier, C. P.; Saykally, R. J.; Shiang, J. J.; Henrichs, S. E.; Heath, J. R. Reversible Tuning of Silver Quantum Dot Monolayers Through the Metal−Insulator Transition. *Science* **1997**, *277*, 1978–1981.

16. Kalsin, A. M.; Fialkowski, M.; Paszewski, M.; Smoukov, S. K.; Bishop, K. J. M.; Grzybowski, B. A. Electrostatic Self-Assembly of Binary Nanoparticle Crystals with a Diamond-Like Lattice. *Science* **2006**, *312*, 420–424.

17. Cheng, W.; Hartman, M. R.; Smilgies, D.-M.; Long, R.; Campolongo, M. J.; Li, R.; Sekar, K.; Hui, C.-Y.; Luo, D. Probing in Real Time the Soft Crystallization of DNA-capped Nanoparticles. *Angew. Chem.* **2010**, *122*, 390–394.

18. Korgel, B. A.; Fullam, S.; Connolly, S.; Fitzmaurice, D. Assembly and Self-Organization of Silver Nanocrystal Superlattices: Ordered "Soft Spheres". *J. Phys. Chem. B* **1998**, *102*, 8379–8388.

19. Dong, A.; Ye, X.; Chen, J.; Murray, C. B. Two-Dimensional Binary and Ternary Nanocrystal Superlattices: The Case of Monolayers and Bilayers. *Nano Lett.* **2011**, *11*, 1804–1809.

20. Nykypanchuk, D.; Maye, M. M.; van der Lelie, D.; Gang, O. DNA-guided Crystallization of Colloidal Nanoparticles. *Nature* **2008**, *451*, 549–552.

21. Park, S. Y.; Lytton-Jean, A. K. R.; Lee, B.; Weigand, S.; Schatz, G. C.; Mirkin, C. A. DNA-Programmable Nanoparticle Crystallization. *Nature* **2008**, *451*, 553–556.

22. Kalsin, A. M.; Grzybowski, B. A. Controlling the Growth of "Ionic" Nanoparticle Supracrystals. *Nano Lett.* **2007**, *7*, 1018–1021.

23. Shevchenko, E. V.; Talapin, D. V.; Murray, C. B.; O'Brien, S. Structural Characterization of Self-assembled Multifunctional Binary Nanoparticle Superlattices. *J. Am. Chem. Soc.* **2006**, *128*, 3620–3637.

24. Leunissen, M. E.; Christova, C. G.; Hynninen, A. P.; Royall, C. P.; Campbell, A. I.; Imhof, A.; Dijkstra, M.; van Roij, R.; Van Blaaderen, A. Ionic Colloidal Crystals of Oppositely Charged Particles. *Nature* **2005**, *437*, 235–240.

25. Campolongo, M. J.; Tan, S. J.; Smilgies, D. M.; Zhao, M.; Chen, Y.; Xhangolli, I.; Cheng, W.; Luo, D. Crystalline Gibbs Monolayers of DNA-capped Nanoparticles at the Air−Liquid Interface. *ACS Nano* **2011**, *5*, 7978–7985.

26. Chen, Y.; Fu, J.; Ng, K.; Tang, Y.; Cheng, W. Free-standing Polymer-Nanoparticle Superlattice Sheets Self-assembled at the Liquid−Air Interface. *Cryst. Growth Des.* **2011**, *11*, 4742–4746.

27. Narayanan, S.; Wang, J.; Lin, X. M. Dynamical Self-Assembly of Nanocrystal Superlattices During Colloidal Droplet Evaporation by *in Situ* Small Angle X-Ray Scattering. *Phys. Rev. Lett.* **2004**, *93*, 135503.

28. Disch, S.; Wetterskog, E.; Hermann, R. P.; Salazar-Alvarez, G.; Busch, P.; Brülckel, T.; Bergström, L.; Kamali, S. Shape Induced Symmetry in Self-assembled Mesocrystals of Iron Oxide Nanocubes. *Nano Lett.* **2011**, *11*, 1651–1656.

29. Jones, M. R.; Macfarlane, R. J.; Lee, B.; Zhang, J.; Young, K. L.; Senesi, A. J.; Mirkin, C. A. DNA-Nanoparticle Superlattices Formed from Anisotropic Building Blocks. *Nat. Mater.* **2010**, *9*, 913–917.

30. Quan, Z.; Fang, J. Superlattices with Non-Spherical Building Blocks. *Nano Today* **2010**, *5*, 390–411.

31. Saunders, A. E.; Ghezelbash, A.; Smilgies, D. M.; Sigman, M. B.; Korgel, B. A. Columnar Self-Assembly of Colloidal Nanodisks. *Nano Lett.* **2006**, *6*, 2959–2963.

32. Nikoobakht, B.; El-Sayed, M. A. Preparation and Growth Mechanism of Gold Nanorods (NRs) Using Seed-mediated Growth Method. *Chem. Mater.* **2003**, *15*, 1957–1962.

33. Nikoobakht, B.; Wang, Z. L.; El-Sayed, M. A. Self-Assembly of Gold Nanorods. *J. Phys. Chem. B* **2000**, *104*, 8635–8640.

34. Hu, X.; Cheng, W.; Wang, T.; Wang, E.; Dong, S. Well-ordered End-to-End Linkage of Gold Nanorods. *Nanotechnology* **2005**, *16*, 2164–2169.

35. Perez-Juste, J.; Pastoriza-Santos, I.; Liz-Marzan, L. M.; Mulvaney, P. Gold Nanorods: Synthesis, Characterization and Applications. *Coord. Chem. Rev.* **2005**, *249*, 1870–1901.

36. Talapin, D. V.; Shevchenko, E. V.; Murray, C. B.; Kornowski, A.; Förster, S.; Weller, H. CdSe and CdSe/CdS Nanorod Solids. *J. Am. Chem. Soc.* **2004**, *126*, 12984–12988.

37. Carbone, L.; Nobile, C.; De Giorgi, M.; Sala, F. D.; Morello, G.; Pompa, P.; Hytch, M.; Snoeck, E.; Fiore, A.; Franchini, I. R.; *et al*. Synthesis and Micrometer-Scale Assembly of Colloidal CdSe/CdS Nanorods Prepared by a Seeded Growth Approach. *Nano Lett.* **2007**, *7*, 2942–2950.

38. Tirado, M. M.; Martnez, C. L.; de la Torre, J. G. Comparison of Theories for the Translational and Rotational Diffusion Coefficients of Rod-Like Macromolecules: Application to Short DNA Fragments. *J. Chem. Phys.* **1984**, *81*, 2047–2052.

39. Hore, M. J. A.; Composto, R. J. Nanorod Self-Assembly for Tuning Optical Absorption. *ACS Nano* **2010**, *4*, 6941–6949.

40. Salski, B.; Celuch, M.; Gwarek, W. FDTD for Nanoscale and Optical Problems. *IEEE Microwave Mag.* **2010**, *11*, 50–59.

41. Kim, S.; Jung, Y. J.; Gu, G. H.; Suh, J. S.; Park, S. M.; Ryu, S. Discrete Dipole Approximation Calculations of Optical Properties of Silver Nanorod Arrays in Porous Anodic Alumina. *J. Phys. Chem. C* **2009**, *113*, 16321–16328.

42. Draine, B. T.; Flatau, P. J. Discrete-Dipole Approximation for Periodic Targets: Theory and Tests. *J. Opt. Soc. Am. A* **2008**, *25*, 2693–2703.

43. Myroshnychenko, V.; Rodrguez-Fernández, J.; Pastoriza-Santos, I.; Funston, A.; Novo, C.; Mulvaney, P.; Liz-Marzan, L.; de Abajo, F. Modelling the Optical Response of Gold Nanoparticles. *Chem. Soc. Rev.* **2008**, *37*, 1792–1805.

44. Prodan, E.; Radloff, C.; Halas, N. J.; Nordlander, P. A Hybridization Model for the Plasmon Response of Complex Nanostructures. *Science* **2003**, *302*, 419–422.

45. Orendorff, C. J.; Murphy, C. J. Quantitation of Metal Content in the Silver-Assisted Growth of Gold Nanorods. *J. Phys. Chem. B* **2006**, *110*, 3990–3994.

46. Yockell-Lelièvre, H.; Desbiens, J.; Ritcey, A. M. Two-Dimensional Self-Organization of Polystyrene-Capped Gold Nanoparticles. *Langmuir* **2007**, *23*, 2843–2850.

47. Corbierre, M. K.; Cameron, N. S.; Lennox, R. B. Polymer-Stabilized Gold Nanoparticles with High Grafting Densities. *Langmuir* **2004**, *20*, 2867–2873.

48. Draine, B. T.; Flatau, P. J. *User Guide for the Discrete Dipole Approximation Code DDSCAT 7.1*, 2010; http://arxiv.org/abs/1002.1505v1

49. Collinge, M. J.; Draine, B. T. Discrete-Dipole Approximation with Polarizabilities that Account for Both Finite Wavelength and Target Geometry. *J. Opt. Soc. Am. A* **2004**, *21*, 2023–2028.

50. Draine, B. T.; Flatau, P. J. Discrete-Dipole Approximation for Scattering Calculations. *J. Opt. Soc. Am. A* **1994**, *11*, 1491–1499.

51. Jackson, J. D. *Classical Electrodynamics*; Wiley: New York, 1998.

52. Draine, B. T. The Discrete-Dipole Approximation and its Application to Interstellar Graphite Grains. *Astrophys. J.* **1988**, *333*, 848–872.

53. Bohren, C. F.; Huffman, D. *Absorption and Scattering of Light by Small Particles*; Wiley: New York, 1983.

54. Coronado, E. A.; Schatz, G. C. Surface Plasmon Broadening for Arbitrary Shape Nanoparticles: A Geometrical Probability Approach. *J. Chem. Phys.* **2003**, *119*, 3926–3934.

55. Vial, A.; Grimault, A. S.; Macas, D.; Barchiesi, D.; de La Chapelle, M. L. Improved Analytical Fit of Gold Dispersion: Application to the Modeling of Extinction Spectra with a Finite-Difference Time-Domain Method. *Phys. Rev. B* **2005**, *71*, 85416.

56. Oubre, C.; Nordlander, P. Optical Properties of Metallodielectric Nanostructures Calculated Using the Finite Difference Time Domain Method. *J. Phys. Chem. B* **2004**, *108*, 17740–17747.